Applied Physics A (2025) 131:91
https://doi.org/10.1007/s00339-024-08206-y

Applied Physics A
Materials Science & Processing

Sintering of inkjet-printed silver nanoparticles by large-area atmospheric pressure nitrogen plasma

Julius Vida[1] · Selen Solak[2] · Yuhang Shao[2] · Tomáš Homola[1,4] · Emil List-Kratochvil[2,3] · Felix Hermerschmidt[2]

Received: 3 September 2024 / Accepted: 18 December 2024 / Published online: 8 January 2025

Abstract
Silver nanoparticles were sintered at atmospheric pressure using nitrogen plasma generated by diffuse coplanar surface barrier discharge (DCSBD). Compared to the standard thermal sintering of 1 h at 140 °C only 8 min of nonthermal plasma treatment at 50 °C were necessary to sufficiently anneal the silver nanoparticle film. Electrical resistivity as low as 9×10^{-6} Ω cm was achieved, i.e., 17% of the bulk conductivity of silver. X-ray photoelectron spectroscopy was used to study the removal of organic moieties from the surface of the inkjet-printed layers. Scanning electron microscopy revealed in detail the process of formation of interconnection between nanoparticles. Our findings pave the way for implementing low-cost and eco-friendly DCSBD plasma sintering into continuous roll-to-roll processing in the future for the annealing of silver nanoparticles on substrates that cannot tolerate high temperatures.

Keywords Plasma sintering · Inkjet printing · Silver nanoparticles · Low-temperature sintering · DCSBD

1 Introduction

Preparation of conductive connections between active components is an essential step in the fabrication of electronic devices. In the field of printed electronics, colloidal dispersions of metal particles are the most widespread, silver being the most widely used material [1]. Numerous techniques have been developed for solution-based deposition including inkjet printing, aerosol printing, slot die coating, screen printing, gravure printing, and many others [2–5].

Among these, inkjet printing stands out due to its industrial scalability, the precision of the printed pattern, small feature size, and minimal waste. It is an additive, non-contact, and highly customizable technique. Thanks to its drop-on-demand character, any digitally generated pattern can be directly realized, with drops only going where required. It is easily scalable and the size of the printed pattern is limited only by the size of the printing area of the printer used [6]. Its digital nature allows simple integration into production lines for future high-throughput yet customizable production of flexible and printed electronic devices [7–10]. Functional coatings are often inkjet-printed using inks containing nanoparticles, however, particle-free inks are also being developed, whose main advantage is the prevention of nozzle clogging [11]. Inkjet-printed devices show promising results for engineering applications in low temperature environments and the devices produced by this technology show stable and repeatable behaviour [12, 13].

Typically, a coating of material deposited from a solution requires an annealing or sintering step to achieve desired material properties. For example, silver nanoparticle inks contain organic solvents, binders and stabilizers that fill the gaps between nanoparticles and prevent agglomeration in the solution. However, when deposited, these organic moieties hinder charge transport across the layer. These components

✉ Felix Hermerschmidt
felix.hermerschmidt@hu-berlin.de

1 CEPLANT-R&D Centre for Plasma and Nanotechnology Surface Modifications, Department of Plasma Physics and Technology, Faculty of Science, Masaryk University, Kotlářská 267/2, 602 00 Brno, Czech Republic

2 Institut für Physik, Institut für Chemie, IRIS Adlershof, Humboldt-Universität zu Berlin, Zum Großen Windkanal 2, 12489 Berlin, Germany

3 Helmholtz-Zentrum Berlin für Materialien und Energie, Hahn-Meitner-Platz 1, 14109 Berlin, Germany

4 Institute of Plasma Physics, Czech Academy of Sciences, U Slovanky 2525/1a, 182 00 Prague 8, Czech Republic

are typically non-volatile, have high boiling points, and often requiring temperatures above 200 °C to remove completely [14]. The composition of the inks can be tuned to lower the necessary temperature, nevertheless, one still finds for most systems that the higher the processing temperature, the better the conductivity of the resulting material.

With the emphasis of the scientific community on the transition to inexpensive, flexible polymer-based substrates [15, 16], the control of the temperature during individual deposition steps has become vital. Some of the commonly used flexible substrates include polyethylene terephthalate (PET) and polyethylene naphthalate (PEN), polyimide (PI), polypropylene (PP), polylactic acid (PLA), etc. Thanks to its good trade-off between price and thermal stability together with good UV resistance, good electrical properties, optical clarity, and gas barrier properties, PET has become a standard flexible substrate for optoelectronic applications. For instance, many commercially available silver nanoparticle ink formulations have been tuned for printing on PET and sintering at 140 °C for 1 h, where PET can retain its mechanical properties [17].

To further reduce the processing temperature and processing times, alternative sintering approaches have been explored [18]. Among the most studied and the most successful is photonic sintering. Electromagnetic radiation from different parts of the spectrum ranging from the visible [19] through infrared [20], to microwave [21], and their combination [22], was successfully used for the sintering of silver nanoparticles. Laser sintering has also been proposed [23, 24]. All of these utilize intensive beams of light that are absorbed by the nanoparticles and locally heat the layer without damaging the underlying substrate.

Sintering by nonthermal plasma has also been previously tested [25, 26], where electrons can reach high temperatures, but the ions and surrounding gas remain at ambient temperature. During plasma sintering, energetic and reactive species from the ionized gas such as electrons, ions, excited and metastable atoms and molecules, as well as photons interact with the treated surface. The polymer chains on the surface break down into smaller volatile fragments, exposing the nanoparticles underneath. As a result, connections form between nanoparticles thanks to large amounts of energy delivered to the surface [27]. Plasma setups operating below atmospheric pressure have a severe disadvantage in requiring cumbersome vacuum chambers and pumping systems incompatible with the desired roll-to-roll processing with high throughput [27–29]. At atmospheric pressure, several authors have experimented with plasma sintering using argon plasma jets [14, 30].

Here, we present the sintering of inkjet-printed silver nanoparticles (Fig. 1a) by plasma generation using diffuse coplanar surface barrier discharge (DCSBD). DCSBD generates macroscopically homogeneous diffuse plasma over a large area by a setup schematically shown in Fig. 1a. This allows for fast treatment of large surfaces. With the highest reported power density among similar atmospheric pressure plasma systems, DCSBD allows for short treatment times. DCSBD has already been applied for fast, low-temperature post-deposition processing of various materials in flexible and printed electronics [31, 32]. Since the DCSBD can be constructed with curved geometry, either convex or concave, it is readily available for incorporation into continuous or roll-to-roll processing (Fig. 1b). DCSBD can operate with nitrogen as a working gas, which is significantly cheaper than previously used argon. The operating temperature can be as low as 50 °C. These advantages make for an excellent eco-friendly alternative for silver nanoparticle sintering.

Lines of silver nanoparticles were inkjet-printed onto PET substrate. Standard thermal sintering and plasma sintering approaches were compared. We characterized the conductivity of the printed lines and used surface characterization techniques to monitor the sintering process. Scanning electron microscopy (SEM) was used for observing the formation of interconnections between the nanoparticles and X-ray photoelectron spectroscopy (XPS) helped elucidate the changes in the surface chemistry after treatment.

2 Method

2.1 Materials, printing, and sintering

Silver nanoparticle ink DGP 40LT-15C from Anapro, with particle size ≤ 50 nm dispersed in triethylene glycol monomethyl ether with a concentration of 30–35 wt%, was purchased from Sigma Aldrich. PET foil with a thickness of 0.1 mm was purchased from Goodfellow Cambridge Ltd. (United Kingdom).

SUSS LP50 research inkjet printer with Spectra SE-128 printhead was used for the printing of silver lines (Fig. 1a). Lines are printed at 635 dpi and at 110 °C substrate temperature with a printing speed of 150 mm/s. The printed layers are dried for 3 min. The printed pattern used for analysis is presented in Figure S1. We printed lines with length 5.8 cm and width varying between 0.3 and 1.6 mm, a total of 8 lines per sample.

After drying, the reference sample was sintered thermally on a hotplate at 140 °C for 1 h. Plasma sintering was done with DCSBD by Roplass (Czech Republic). DCSBD is based on the principle of dielectric barrier discharge (DBD) with the coplanar arrangement of interdigitated electrodes embedded in an alumina ceramic (Fig. 1a). A detailed description of the DCSBD plasma source can be found elsewhere [33, 34]. Thanks to the coplanar arrangement of the electrodes, the plasma is generated in a thin layer (~0.3 mm) on top of a 10 cm × 8 cm ceramic. The input power was 200 W, resulting

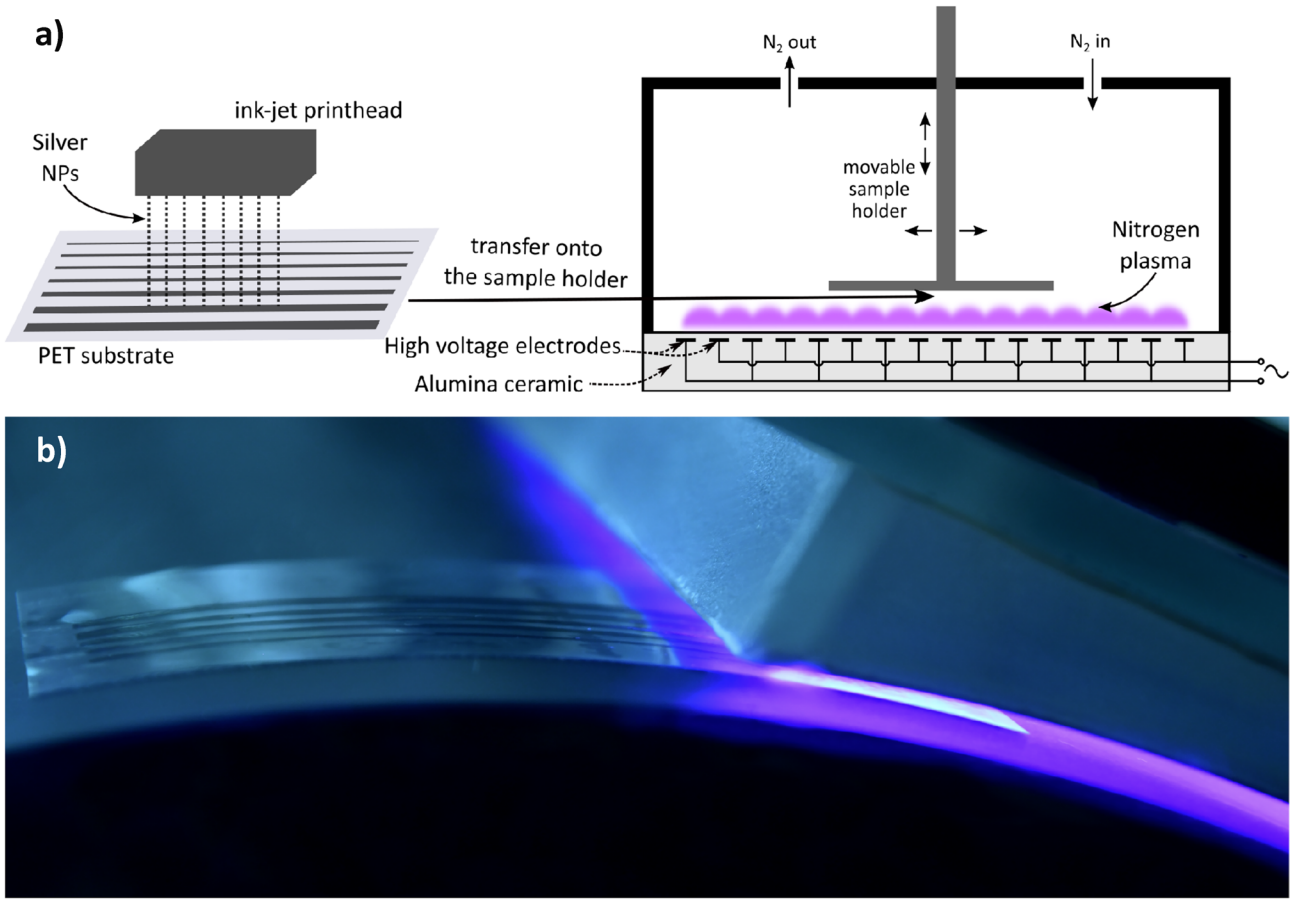

Fig. 1 **a** Inkjet printing of silver nanoparticles on PET flexible substrate and a scheme of the flat diffuse coplanar surface barrier discharge (DCSBD) unit with a chamber for treatment in nitrogen. The sample with printed lines of silver nanoparticles is mounted on a sample holder using tape. **b** A photo of the roll-to-roll setup for surface modification by diffuse coplanar DCSBD with curved geometry

in a high power density of 2.5 W/cm^2, which is typical for DCSBD. A simple gas chamber with a volume of 0.7 L with a gas inlet and outlet was used to operate the DCSBD with nitrogen as a working gas (Fig. 1a). The nitrogen flow was set to 1.4 L/min during the sintering process. The dried samples were transferred onto a sample holder and secured with double-sided tape (Fig. 1a). Prior to the treatment, the chamber was flushed with nitrogen for two minutes to remove oxygen from the chamber. The sample was lowered using a sample holder to the working distance of 0.3 mm from the ceramic to maintain contact with the plasma region. The 0.3 mm working distance was ensured with a thin piece of polyimide tape. To ensure a homogeneous treatment of the sample, the sample holder was moved horizontally over the plasma region during treatment. The treatment time was 1, 2, 4, 8, and 16 min and the temperature of the ceramic was maintained at 50 °C, measured using a temperature sensor embedded in the ceramic of the DCSBD plasma unit and cooled with a fan.

We compared the conductivity of the dried untreated sample with the thermally sintered sample and the plasma-treated samples with varying treatment time. The silver lines were printed on PET as well as on soda-lime glass for comparison of conductivity. For chemical and structural analyses, the large samples were cut across the printed silver lines to prepare smaller samples. There were eight lines on the sample allowing measurement of multiple points on the sample for statistics.

2.2 Surface characterization

The electrical resistance of the printed lines was measured using a two-point method with a multimeter (Fluke 179). The results were compensated for the contact resistance of the multimeter of 0.2 Ω. The resistivity was calculated using the resistance and the dimensions of the printed lines. The lines were 5.8 cm long. The line thickness and the line width were determined from the profiles measured using a DektakXT profilometer from Bruker (USA). The width of the lines varied between 0.3 and 1.6 mm. The thickness of the lines was consistent around (1 ± 0.2) µm.

XPS was used in this study with the aim of analysing the elemental composition and the chemical bonding on the surface of the studied samples. The spectrometer was an Axis Supra from Kratos Analytical Ltd. (United Kingdom). The base pressure during spectra acquisition was better than 6×10^{-7} mbar. The excitation source was monochromated Al Kα spectral line with an energy of 1486.3 eV. The recorded spectra include survey spectra and core-level spectra. The survey spectra were collected with a pass energy of 80 eV and the core-level spectra with a pass energy of 20 eV. The samples were attached to the holder using copper clamps to secure good electrical contact between the sample and the spectrometer. No charge neutralizing was used. CasaXPS software was used for data processing and quantification. Two points were measured for each experimental condition.

SEM was used to study the morphology of the samples. The top view SEM images were taken with a GeminiSEM 500 from Zeiss Microscopy (Germany). An accelerating voltage of 15 kV was used and images were captured in the in-beam secondary electron imaging mode with working distance (5.0 ± 0.2) mm. For the cross-section imaging, the samples were prepared by cutting and breaking larger samples across the printed silver lines on glass. The samples were then inserted sideways into a Mira3 SEM from Tescan (Czech Republic). An accelerating voltage of 10 kV and a working distance (5.0 ± 0.2) mm was used. Images were captured in both in-beam secondary electron and in-beam backscattered electron imaging modes. Samples were secured using metal clamps to ensure good electrical contact.

3 Results and discussion

The inkjet-printed lines of silver nanoparticles of various width ranging from 0.3 to 1.6 mm were dried and sintered thermally using nitrogen plasma. The top-view under a confocal microscope of the lines sintered thermally and by plasma for various duration is shown in Fig. 2. The profiles of printed lines are shown in Figure S2. The thickness of the lines was consistent around (1 ± 0.2) µm regardless of the line width or sintering method. The measured width and thickness of the printed lines for various sintering conditions are presented in Table S1 and S2. The width of the lines influenced the profile of the lines. The cross-sectional profile of the lines with a width between 0.3 and 0.8 mm was concave due to the coffee ring effect [35]. The widest lines at 1.6 mm across had a convex profile. The lines in between with widths between 0.8 and 1.2 mm were flat. The cross-sectional profile has been shown to be dependent on the drying conditions, specifically humidity and drying time [36]. The cross-sectional profile was the same for thermally sintered and plasma-sintered lines and the plasma-sintering time did not affect the profile either.

Figure 3 shows the resulting resistivity of the silver nanoparticles sintered by plasma for various duration calculated from the dimensions of the lines and measured resistance presented in Table S3 and S4. The resistivity of the dried sample without any sintering was $(9\pm1)\times10^{-5}$ Ω cm. Immediately after treatment in plasma for 1 min, the resistivity dropped to $(2\pm0.2)\times10^{-5}$ Ω cm. The lowest resistivity was achieved after 8 min of sintering at $(9\pm1)\times10^{-6}$ Ω cm and did not improve further with longer sintering time. For comparison, the sample with standard thermal sintering at 140 °C for 1 h reached resistivity of $(10\pm2)\times10^{-6}$ Ω cm. The bulk resistivity of silver is 1.6×10^{-6} Ω cm at 20 °C.

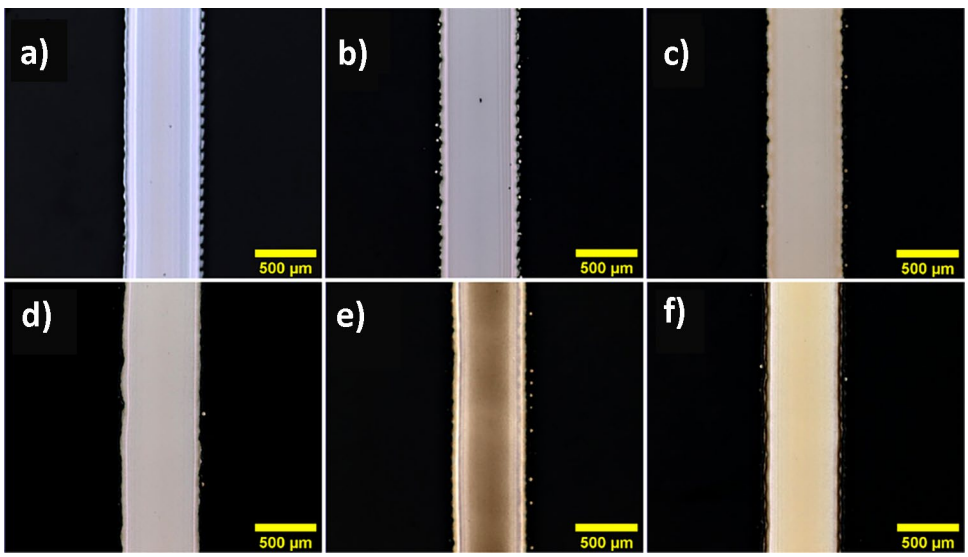

Fig. 2 Microscope images showing the printed nanoparticle lines on glass **a** dried at 110 °C, **b** thermally sintered at 140 °C for 1 h, and plasma-sintered for **c** 1 min, **d** 2 min, **e** 4 min and **f** 8 min

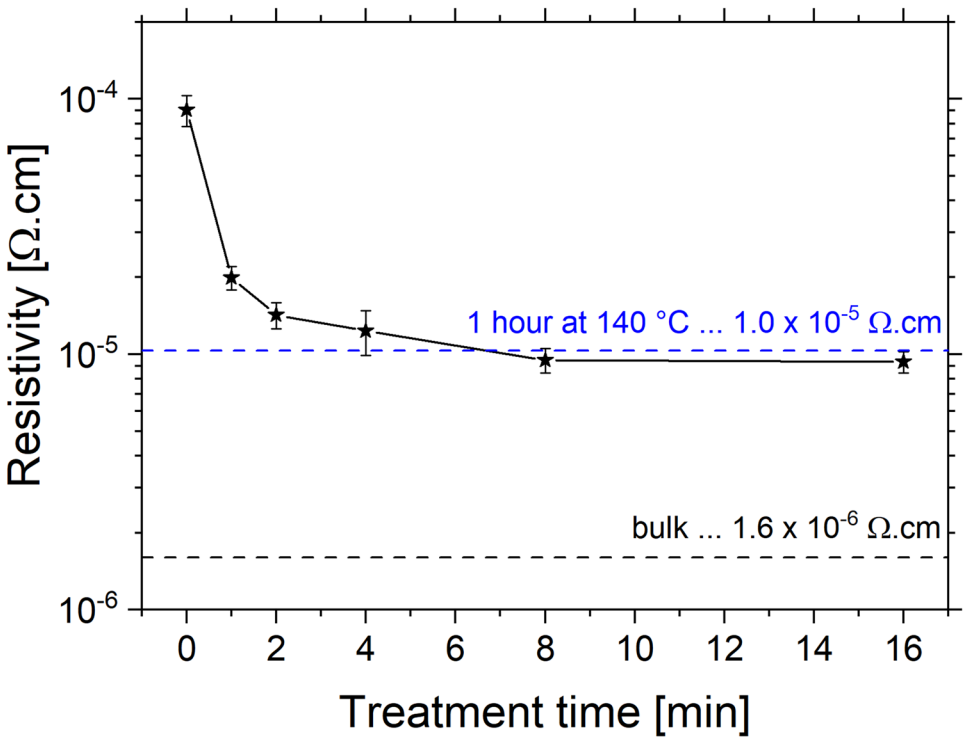

Fig. 3 Resistivity of the inkjet-printed silver nanoparticle lines on PET as a function of plasma treatment time compared to the standard thermal sintering process at 140 °C for 1 h. The resistivity does not decrease for treatment longer than 8 min

The conductivity of the best plasma-sintered samples was (17 ± 2)% of the bulk conductivity of silver compared to (16 ± 2)% for the thermal sintering. We see that the same value was achieved after just 8 min at 50 °C compared to 1 h at 140 °C. For comparison, the achieved resistivity and conductivity values on glass are shown in Figure S3 and S4.

Two important mechanisms are responsible for the improved electrical conductivity of printed nanoparticles during sintering. First, the organic components of the ink are removed from the spaces between nanoparticles, allowing the nanoparticles to make direct contact. Consequently, larger particles are formed at the expense of smaller particles due to the reduction of surface energy and so-called necks with increasingly larger radii form between nanoparticles [37]. This process is called Ostwald ripening [38, 39], and characterized by the dissolution of smaller nanoparticles, which possess higher surface energy due to their curvature, followed by the redeposition of atoms onto larger nanoparticles, leading to their growth. The driving force behind Ostwald ripening is the reduction in total system free energy, as larger particles are thermodynamically more stable than smaller ones. This coarsening mechanism is crucial in determining the electrical conductivity of the sintered silver films, as larger, interconnected grains provide lower electrical resistance paths [40]. In other words, the better the connections, the closer the properties of the coatings get to those of the bulk material.

The removal of the organic moieties from the material can be monitored by the changes in the surface chemistry induced by the sintering. XPS revealed that the surface of the dried sample without sintering contained 24% silver, 57% carbon, 12% oxygen and 6% nitrogen (see Table S5). After plasma sintering, the carbon content dropped to around 33% and the silver content increased to around 55%. The oxygen content remained the same and there was no nitrogen detected on the surface.

To elucidate the changes in surface chemistry, we analysed the core-level XPS spectra. Figure 4a compares the C 1*s* region measured on the dried sample, thermally sintered sample and sample sintered by plasma for 8 min. We observed that aside from the signal from adsorbed carbohydrates between 284 and 285 eV, the dried sample and thermally sintered sample contained a significant contribution at around 286 eV from C–OH and C–O–C groups. This signal presumably originates from the triethylene glycol monomethyl ether solvent that was not evaporated completely. There are also smaller contributions at around 287.5 eV and 288.5 eV, typically assigned to carbonyl (C=O) and carboxyl (O–C=O) groups [41]. After plasma treatment, we observed almost complete removal of the signal from hydroxyl and ether groups from the solvent. The only remaining signal can be attributed to adsorbed hydrocarbons on the surface. There is also a smaller contribution from carbonyl groups. The presence of adsorbed carbon species was expected, since the samples were handled and transported in ambient conditions. Similarly, the O 1*s* spectra in Fig. 4b show a significant decrease in the signal between 532 and 534 eV after plasma sintering, where the signal from

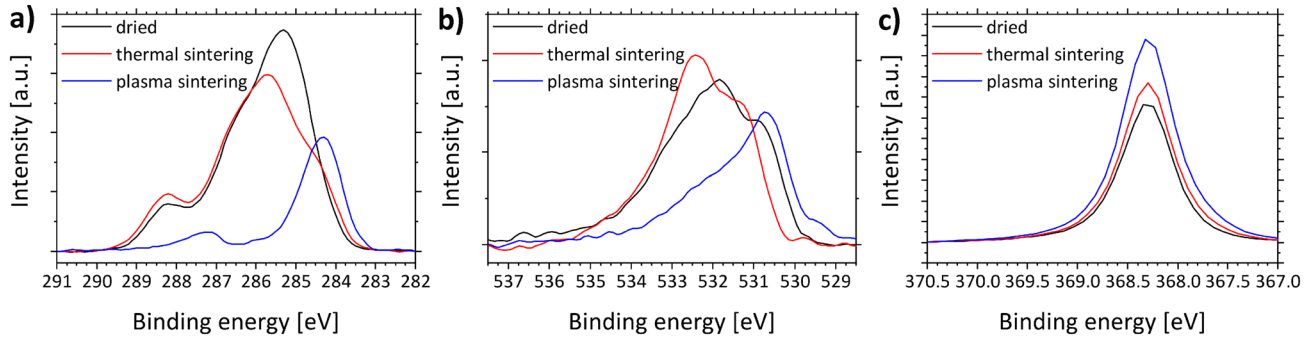

Fig. 4 Comparison of **a** C 1*s*, **b** O 1*s* and **c** Ag 3*d* 5/2 core-level XPS spectra for dried, thermally sintered and plasma sintered for 8 min (optimal treatment time) printed silver nanoparticles on PET

oxygen single-bound to carbon usually contributes. The O 1*s* spectrum is considerably harder to interpret since numerous atomic environments contribute to a narrow interval of binding energies. The Ag 3*d* 5/2 core-level spectra in Fig. 4c display a narrow peak of metallic silver cantered around 368.3 eV, corresponding well with the literature values [42]. The signal intensifies after thermal sintering and even more after plasma sintering. There is no significant shift in binding energies or broadening of the peak observed. The results of the chemical analysis of the surface of sintered silver nanoparticles show that by plasma treatment the organic parts of the ink were removed faster and more thoroughly than by thermal annealing (see Figure S5). Removal of the organic stabilizers and binders is a crucial step to initiate agglomeration of nanoparticles which leads to direct contact and growth of nanoparticles [35].

A simple way to observe the interconnection of nanoparticles is to view them by SEM. In Fig. 5, surfaces of six samples with different post-deposition processing are shown. Figure 5a shows nanoparticles after drying at 110 °C for 10 min without any sintering procedure. The gaps between individual nanoparticles are clearly visible. This lack of interconnection hinders the transfer of charge across the layer. After standard thermal sintering at 140 °C for 1 h (Fig. 5b), necks formed connecting neighbouring nanoparticles. Figure 5c–f show the surface of samples with nanoparticles sintered by plasma for 1, 2, 4, and 8 min, respectively. The connections between nanoparticles on the surface are clearly visible after just 1 min of sintering. With prolonged plasma exposure, we observed the widening of the necks and gradual growth of nanoparticles, until after 8 min of treatment the nanoparticles joined together in a continuous film.

The cross-sectional view of the dried sample with nanoparticles without sintering in Figure S6a confirms discrete nanoparticles throughout the layer. The cross-section of thermally sintered nanoparticle film in Figure S6b shows the

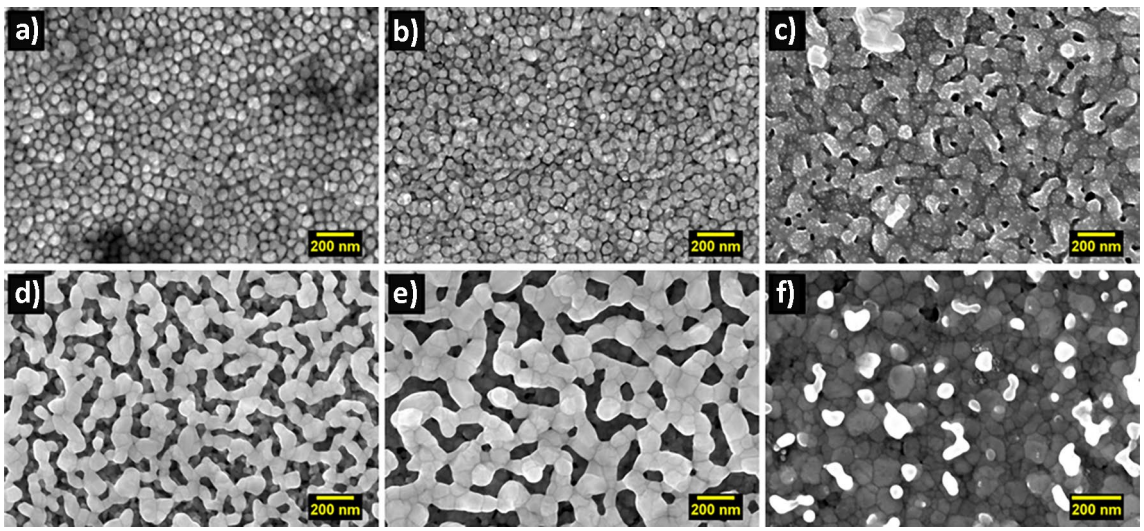

Fig. 5 Scanning electron microscopy images showing the surface of printed nanoparticle lines on glass **a** dried at 110 °C, **b** thermally sintered at 140 °C for 1 h, and plasma-sintered for **c** 1 min, **d** 2 min, **e** 4 min and **f** 8 min

interconnection of nanoparticles into larger structures, which is beneficial for easier charge transfer. The cross-sectional view of the sample with plasma-sintered nanoparticles in Figure S6c also displays interconnection between nanoparticles deeper in the film, however to a much lesser degree than the thermally sintered sample. The top layer of the sample, however, formed a continuous silver film, similar to the results observed by previous studies [11, 14, 16].

4 Conclusion

Atmospheric pressure nonthermal plasma in nitrogen of the DCSBD was used for sintering of inkjet-printed silver nanoparticles on PET substrate. After sintering for only 1 min the resistivity of the material rapidly dropped and the lowest resistivity of $(9 \pm 1) \times 10^{-6}$ Ω cm was achieved after 8 min of plasma treatment at just 50 °C, which translates to around 17% of the bulk conductivity of silver. For comparison, standard thermal annealing at 140 °C for 1 h resulted in a resistivity of $(1.0 \pm 0.2) \times 10^{-5}$ Ω cm, i.e. around 16% of the bulk conductivity of silver. XPS revealed efficient removal of C–O–C and C–OH groups from the triethylene glycol monomethyl ether solvent immediately after plasma exposure. These species were still present in large quantities on the surface of thermally treated samples. SEM imaging revealed in detail the morphological changes induced by sintering. Compared to the surface of a dried sample, where discrete nanoparticles were observed, the plasma-sintered nanoparticles formed interconnections between each other and after a prolonged plasma exposure for 8 min, a continuous silver layer formed on the surface of the film. These results show promise for the use of DCSBD plasma for rapid sintering of silver nanoparticles on temperature-sensitive substrates for inline processes in large area roll-to-roll fabrication.

Supplementary Information The online version contains supplementary material available at https://doi.org/10.1007/s00339-024-08206-y.

Acknowledgements This research was supported by projects LM2023039 and LM2023051 funded by the Ministry of Education, Youth, and Sports of the Czech Republic. The research was also supported by the Internal Grant Agency of Masaryk University project registration number CZ.02.2.69/0.0/0.0/19_073/0016943. The work was conducted in the framework of the Joint Lab GEN_FAB and was supported by the HySPRINT innovation lab at Helmholtz-Zentrum Berlin.

Author contributions All authors contributed to the study conception and design. Material preparation, data collection and analysis were performed by Julius Vida, Selen Solak and Yuhang Shao. The first draft of the manuscript was written by Julius Vida and reviewed and edited by Julius Vida, Felix Hermerschmidt, Emil List-Kratochvil and Tomáš Homola. All authors read and approved the final manuscript.

Funding Open Access funding enabled and organized by Projekt DEAL.

Data availability All data is available within this manuscript and the supporting information.

Declarations

Conflict of interest The authors declare no competing interest.

References

1. N. Ibrahim, J.O. Akindoyo, M. Mariatti, J. Sci. Adv. Mater. Devices. **7**(1), 100395 (2022). https://doi.org/10.1016/J.JSAMD.2021.09.002
2. K.S. Kwon, M.K. Rahman, T.H. Phung, S.D. Hoath, S. Jeong, J.S. Kim, Flex. Print. Electron. **5**(4), 043003 (2020). https://doi.org/10.1088/2058-8585/ABC8CA
3. M. Smith, Y.S. Choi, C. Boughey, S. Kar-Narayan, Flex. Print. Electron. **2**(1), 015004 (2017). https://doi.org/10.1088/2058-8585/AA5AF9
4. G. Grau, J. Cen, H. Kang, R. Kitsomboonloha, W.J. Scheideler, V. Subramanian, Flex. Print. Electron. **1**(2), 023002 (2016). https://doi.org/10.1088/2058-8585/1/2/023002
5. F. Hermerschmidt, S.A. Choulis, E.J.W. List-Kratochvil, Adv. Mater. Technol. **4**, 1800474 (2019). https://doi.org/10.1002/admt.201800474
6. V.R.F. Schröder, N. Fratzscher, F. Mathies, E.R. Nandayapa, F. Hermerschmidt, E.L. Unger, E.J.W. List-Kratochvil, Nanoscale **15**(12), 5649–5654 (2023). https://doi.org/10.1039/d3nr00565h
7. B. Wilk, S. Sahayaraj, M. Ziółek, V. Babu, R. Kudrawiec, K. Wojciechowski, Adv. Mater. Technol. **7**(12), 1–12 (2022). https://doi.org/10.1002/admt.202200606
8. L. Kinner, S. Nau, K. Popovic, S. Sax, I. Burgués-Ceballos, F. Hermerschmidt, A. Lange, C. Boeffel, S.A. Choulis, E.J.W. List-Kratochvil, Appl. Phys. Lett. (2017). https://doi.org/10.1063/1.4978429
9. S. Gamerith, A. Klug, H. Scheiber, U. Scherf, E. Moderegger, E.J.W. List, Adv. Funct. Mater. **17**(16), 3111–3118 (2007). https://doi.org/10.1002/adfm.200600762
10. H. Sirringhaus, T. Kawase, R.H. Friend, T. Shimoda, M. Inbasekaren, W. Wu, E.P. Woo, Science (80-) **290**(December), 2123–2127 (2000). https://doi.org/10.1126/science.290.5499.2123
11. W. Yang, E.J.W. List-Kratochvil, C. Wang, J. Mater. Chem. C. **7**(48), 15098–15117 (2019). https://doi.org/10.1039/c9tc05463d
12. C. Acosta, W.P. Flynn, S. Garnsey, W. Dipon, R. Guo, A. Bhalla, Sens. Actuators A Phys. **374**(16), 115483 (2024). https://doi.org/10.1016/j.sna.2024.115483
13. J. Jäger, A. Schwenck, D. Walter, A. Bülau, K. Gläser, A. Zimmermann, Sensors **22**(21), 8145 (2022). https://doi.org/10.3390/s22218145

14. N. Turan, M. Saeidi-Javash, J. Chen, M. Zeng, Y. Zhang, D.B. Go, A.C.S. Appl, Mater. Interfaces (2021). https://doi.org/10.1021/acsami.1c14049
15. P. Martins, N. Pereira, A.C. Lima, A. Garcia, C. Mendes-Filipe, R. Policia, V. Correia, S. Lanceros-Mendez, Adv. Funct. Mater. (2023). https://doi.org/10.1002/adfm.202213744
16. S.M.F. Cruz, L.A. Rocha, J.C. Viana, in *Flexible Electronics*, ed. by S. Rackauskas (InTech, London, 2018)
17. W.A. MacDonald, M.K. Looney, D. MacKerron, R. Eveson, R. Adam, K. Hashimoto, K. Rakos, J. Soc. Inf. Disp. **15**(12), 1075 (2007). https://doi.org/10.1889/1.2825093
18. A. Hussain, H.L. Lee, S.J. Moon, Mater. Today Commun. **2023**(34), 105159 (2022). https://doi.org/10.1016/j.mtcomm.2022.105159
19. J.S. Kang, J. Ryu, H.S. Kim, H.T. Hahn, J. Electron. Mater. **40**(11), 2268–2277 (2011). https://doi.org/10.1007/S11664-011-1711-0/METRICS
20. J. Park, H.J. Kang, K.-H. Shin, H. Kang, Nat. Publ. Gr. (2016). https://doi.org/10.1038/srep34470
21. J. Perelaer, B.J. De Gans, U.S. Schubert, Adv. Mater. **18**(16), 2101–2104 (2006). https://doi.org/10.1002/adma.200502422
22. H.J. Hwang, K.H. Oh, H.S. Kim, Sci. Rep. **6**(1), 1–10 (2016). https://doi.org/10.1038/srep19696
23. A. Sharif, N. Farid, G.M. O'Connor, Results Eng. **16**, 100731 (2022). https://doi.org/10.1016/J.RINENG.2022.100731
24. S.M. Pozov, G. Schider, S. Voigt, F. Ebert, K. Popovic, F. Hermerschmidt, E. Georgiou, I. Burgués-Ceballos, L. Kinner, D. Nees et al., Flex. Print. Electron. (2019). https://doi.org/10.1088/2058-8585/ab17a5
25. M. Hengge, K. Livanov, N. Zamoshchik, F. Hermerschmidt, E.J.W. List-Kratochvil, Flex. Print. Electron. **6**(1), 15009 (2021). https://doi.org/10.1088/2058-8585/abe604
26. W. Yang, F. Hermerschmidt, F. Mathies, E.J.W. List-Kratochvil, J. Mater. Sci. Mater. Electron. **32**(5), 6312–6322 (2021). https://doi.org/10.1007/s10854-021-05347-1
27. S. Ma, V. Bromberg, L. Liu, F.D. Egitto, P.R. Chiarot, T.J. Singler, Appl. Surf. Sci. **293**, 207–215 (2014). https://doi.org/10.1016/J.APSUSC.2013.12.135
28. I. Reinhold, C.E. Hendriks, R. Eckardt, J.M. Kranenburg, J. Perelaer, R.R. Baumann, U.S. Schubert, J. Mater. Chem. **19**(21), 3384–3388 (2009). https://doi.org/10.1039/B823329B
29. F.M. Wolf, J. Perelaer, S. Stumpf, D. Bollen, F. Kriebel, U.S. Schubert, J. Mater. Res. **28**(9), 1254–1261 (2013). https://doi.org/10.1557/JMR.2013.73
30. S. Wünscher, S. Stumpf, A. Teichler, O. Pabst, J. Perelaer, E. Beckert, U.S. Schubert, J. Mater. Chem. **22**(47), 24569–24576 (2012). https://doi.org/10.1039/c2jm35586h
31. M. Shekargoftar, J. Pospisil, M. Kratochvíl, J. Vida, P. Souček, T. Homola, Energy Technol. **9**(5), 1–7 (2021). https://doi.org/10.1002/ente.202001076
32. T. Homola, J. Pospisil, M. Shekargoftar, T. Svoboda, M. Hvojnik, P. Gemeiner, M. Weiter, P. Dzik, A.C.S. Appl, Energy Mater. **3**(12), 12009–12018 (2020). https://doi.org/10.1021/acsaem.0c02144
33. M. Černák, L. Černáková, I. Hudec, D. Kováčik, A. Zahoranová, EPJ Appl. Phys. **47**(2), 1 (2009). https://doi.org/10.1051/epjap/2009131
34. T. Homola, J. Matoušek, M. Kormunda, L.Y.L. Wu, M. Černák, Plasma Chem. Plasma Process. **33**(5), 881–894 (2013). https://doi.org/10.1007/s11090-013-9467-3
35. D. Mampallil, H.B. Eral, Adv. Colloid Interface Sci. **252**, 38–54 (2018). https://doi.org/10.1016/j.cis.2017.12.008
36. K. Fukuda, T. Sekine, D. Kumaki, S. Tokito, ACS Appl. Mater. Interfaces **5**(9), 3916–3920 (2013). https://doi.org/10.1021/am400632s
37. J. Perelaer, U.S. Schubert, J. Mater. Res. **28**(4), 564–573 (2013). https://doi.org/10.1557/jmr.2012.419
38. Y. Tang, W. He, S. Wang, Z. Tao, L. Cheng, CrystEngComm **16**, 4431 (2014). https://doi.org/10.1039/c3ce42439a
39. S.R. Challa, A.T. Delariva, T.W. Hansen, S. Helveg, J. Sehested, P.L. Hansen, F. Garzon, A.K. Datye, J. Am. Chem. Soc. (2011). https://doi.org/10.1021/ja208324n
40. R. Ouyang, J. Liu, W. Li, J. Am. Chem. Soc. **135**(5), 1760–1771 (2013). https://doi.org/10.1021/ja3087054
41. T.R. Gengenbach, G.H. Major, M.R. Linford, C.D. Easton, J. Vac. Sci. Technol. A Vac. Surf. Film **1**(1), 013204 (2021). https://doi.org/10.1116/6.0000682
42. P. Prieto, V. Nistor, K. Nouneh, M. Oyama, M. Abd-Lefdil, R. Díaz, Appl. Surf. Sci. **22**(258), 8807–8813 (2012). https://doi.org/10.1016/j.apsusc.2012.05.095